Composites Communications 23 (2021) 100600

Contents lists available at ScienceDirect

Composites Communications

journal homepage: www.elsevier.com/locate/coco

3D printing of polycaprolactone-based composites with diversely tunable mechanical gradients via multi-material fused deposition modeling

Xu Zhang [a], Jianlei Wang [b,*], Tianxi Liu [a,c,**]

[a] Innovation Center for Textile Science and Technology, State Key Laboratory for Modification of Chemical Fibers and Polymer Materials, College of Materials Science and Engineering, Donghua University, Shanghai, 201620, PR China
[b] CAS Key Laboratory of Design and Assembly of Functional Nanostructures, and Fujian Key Laboratory of Nanomaterials, Fujian Institute of Research on the Structure of Matter, Chinese Academy of Sciences, Fuzhou, Fujian, 350002, PR China
[c] Key Laboratory of Synthetic and Biological Colloids, Ministry of Education, School of Chemical and Material Engineering, Jiangnan University, Wuxi, 214122, PR China

ARTICLE INFO

Keywords:
Functionally gradient materials
Mechanical gradients
Fused deposition modeling
3D printing

ABSTRACT

The developed multi-material fused deposition modeling (*m*-FDM) 3D printing approach was proposed to fabricate functionally gradient composites (FGCs) with diversely tunable mechanical gradients. The mechanical properties of the *m*-FDM 3D printed FGCs were studied as a whole part, including the interlaminar shear strength (ILSS), the storage modulus, and the tensile strength. The interlaminar shear testing results convinced that the loading direction plays a crucial importance in determining the overall mechanical strength. Furthermore, the FGCs with different linear continuous gradients of filler content were prepared to examine the relationship between structures and properties of the FGCs. In addition, the porosity of the *m*-FDM 3D printed parts was also presented to demonstrate the mechanism behind the effect of the gradient of filler content on the whole mechanical properties. Finally, a potential application as the intermediated layers between two different materials to prevent warping and spalling when heating and achieve the optimal effect of the heat and stress transfer simultaneously. The present study elaborates on the relationship between structures and properties of FGCs, which also helps to establish a theoretical foundation of the practical applications in diverse fields.

1. Introduction

In nature, most organism structures are made of several distinguishing materials with a significantly hierarchical difference in the properties [1,2]. To adapt the multiple functions at each local part of an organism, the distribution of a particular functional component or structure should change gradually in one or more directions across space [3,4]. Similar to the principle of the natural materials, the so-called functionally gradient material (FGM) is composed of a synergistic combination of different materials with a gradual change in the composition or structure, leading to a gradient change in the properties [5–7]. The gradient of composition, structures, as well as properties at the local scale gifts FGMs with the capacity to enable actual applications in various fields [8–10]. Functionally gradient composite (FGC) with mechanical gradients is a typical kind of FGM, which can effectively distribute stress acting on the material at interfaces to alleviate the damage to itself [11]. However, the fabrication of FGCs suffers from shortcomings in control of the gradient continuity and tunability, while the formation mechanism of the functional gradients is also not clear.

Additive manufacturing (AM) or 3D printing (3DP) is most beneficial in fabricating the parts or products with complex and tailored designs [7,12–14]. Based on the advantages in control of structures, resolution, and scalability, etc., 3D printing of FGMs with widely and diversely tunable properties in a single 3D printing process gradually grows in significance and has been energetically studied recently. Kuang et al. [15] presented a 3D printing method based on the grayscale digital light processing (g-DLP) to obtain FGMs with high-resolution and widely tunable mechanical gradients, where the two-stage curing ink and the grayscale light patterns were conjunctively used. Otherwise, Mirzaali et al. [16] designed the FGMs with step-wise and continuous gradients

* Corresponding author.
** Corresponding author. Innovation Center for Textile Science and Technology, State Key Laboratory for Modification of Chemical Fibers and Polymer Materials, College of Materials Science and Engineering, Donghua University, Shanghai, 201620, PR China.
E-mail addresses: jlwang@fjirsm.ac.cn (J. Wang), txliu@dhu.edu.cn, txliu@jiangnan.edu.cn (T. Liu).

https://doi.org/10.1016/j.coco.2020.100600
Received 25 October 2020; Received in revised form 15 December 2020; Accepted 15 December 2020

via the voxel-based multi-material 3D printing technology, revealing that the FGMs with linear gradients perform better stiffness and strength than the step-wise gradients. Among the severally mentioned AM or 3DP technologies, the extrusion-based 3D printing approach is best noted for its simplicity, low cost, scalable manufacturing, and wide material choices [7,12,17–20]. Thus, on account of the multi-material extrusion-based 3D printing technology, Giachini et al. [21] successfully established a combined method to build the cellulose-based tunable viscoelastic materials with continuous and multi-functional gradients by uniting the materials engineering with the digital processing.

In our previous work [7], we have developed a 3D printing approach based on multi-material fused deposition modeling (*m*-FDM) to fabricate the FGCs with anisotropic thermal conductivity or conductive properties. The relationship between structures and thermal conductive properties of the FGC parts was reasonably established. In the present study, we would further examine the mechanical properties of FGCs via *m*-FDM 3D printing based on our previous work [7]. The mechanical properties of the fabricated samples, including the interlaminar shear strength (ILSS), the storage modulus, and the tensile strength, were demonstrated as a whole part, and then the relationship between structures and mechanical properties was further explored, which established the theoretical basis for further practical applications in various fields. Ultimately, one potential application of the designed thermoplastic FGCs as the intermediate layers between two incompatible materials (e.g. Al foil and PVC film) with a huge difference in the thermal expansion coefficient was proposed to improve the interfacial adhesion or bonding strength and reduce the residual stress which primarily cracks the materials.

2. Experimental section

2.1. Material preparation

In the present study, the polycaprolactone (PCL) was produced by Perstorp Co. The 30 μm (particle size) aluminum nitride (AlN-30) and 30 μm (particle size) boron nitride (BN-30) were introduced into the PCL matrix to prepare the PCL-based composite filaments for the *m*-FDM 3D printing. The preparation of the filaments comprises three procedures: (1) The powders (AlN-30 and BN-30) were treated with silane coupling agent 3-aminopropyltriethoxysilane (APTS) to strengthen the interface bonding interactions with polycaprolactone (PCL) and prevent oxidization and hydrolyzation during preparation. (2) The mixtures were mixed with PCL for 5 min and then compounded in HAAKE twin-screw extruder to prepare masterbatches. The content of the powders (AlN-30 and BN-30) was 80 wt%. (3) The masterbatches and the different contents of PCL were mixed and then extruded in a single-screw extruder to prepare filament with 1.75 mm in diameter. During the extruding process, the barrel temperature ranged between 70 °C and 90 °C.

2.2. 3D printing via multi-material fused deposition modeling

As shown in Scheme 1, the heating chamber of the *m*-FDM 3D printer has two channels and one nozzle, which can make two components mix in the merging area and then come out as one deposited line. Simultaneously, two high-power stepper motors were applied to ensure printing stability and accuracy. The microscopic uniformity can be realized through the shear effect coming from the inner structure. The motor speed can be controlled respectively through software to adjust feeding rate to achieve arbitrary proportion of components in the deposited line, which helps to achieve macroscopic heterogeneity. During the *m*-FDM 3D printing process, the nozzle temperature was maintained at 100 °C, while the platform temperature was near room temperature. The layer height and the infill density were set to be 0.2 mm and 100%, respectively. The nozzle diameter of the FDM unit was 0.4 mm, ensuring that no clogging would happen. The printing speed for the first layer and the other layers were 30 and 50 mm/s, respectively. In the *m*-FDM 3D printing process, the filaments as feedstocks were fed into the heating chamber by stepping motor and extruded through the nozzle in a prescribed manner upon its melting temperature, then solidified and deposited on the platform on a layer-by-layer basis.

2.3. Characterization

The *m*-FDM 3D printed specimens were performed on a universal testing machine (AGS-X Shimadzu Co., Kyoto, Japan) with a 1 kN transducer capacity. The ISO 527 standard (5A dog-bone dimensions) and ISO 14130 standard (rectangular bar dimensions) were followed for the tensile and ILSS test, respectively. The cross-head speed for the tensile and interlaminar shear testing was 5 mm/min and 2 mm/min, respectively. The dynamic mechanical analysis (DMA) was carried out between 25 °C and 60 °C (heating rate: 5 °C/min) with storage modulus G′ recorded concerning temperature on the DMA Q800 (TA Co., New Castle, USA) under the single cantilever approach. The SEM fractured surface morphologies were observed by Hitachi SU8010 FEG-SEM with 5 kV acceleration voltage after fracturing in liquid nitrogen.

The porosity (*P*) of the *m*-FDM 3D printed specimens can be given by [22].

$$P = \frac{V_t - V_a}{V_t} \times 100\%$$

where the V_t and V_a represent the dimensionally calculated volume and the actually measured volume of the specimens, respectively. Although the volume of designed solid object can be directly calculated by 3D modeling software, the shrinkage of material and printing accuracy error of FDM machine may affect the result. To measure V_t accurately, the rectangular samples with 2 mm in shell thickness were prepared to ensure on open pore and the Archimedes approach was adopted. The actually measured volume, V_a, can be calculated as follows

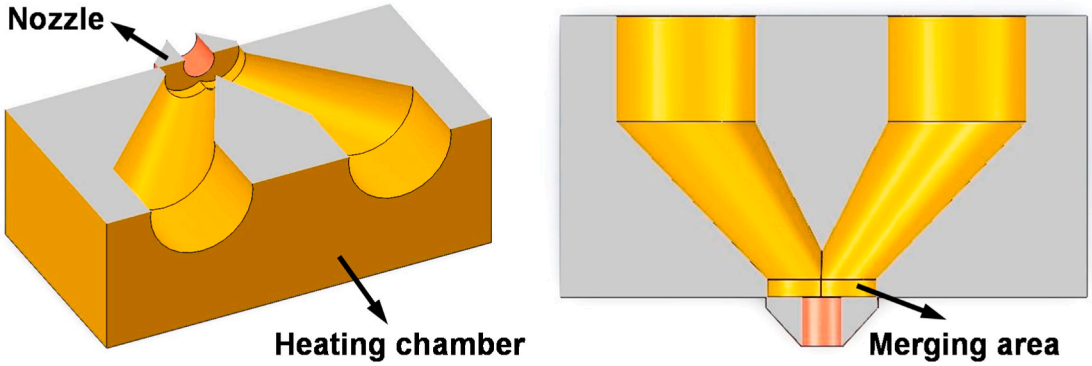

Scheme 1. Schematic illustration of the heating chamber of the *m*-FDM 3D printer.

$$V_a = \frac{m \times c_{PCL}}{\rho_{PCL}} + \frac{m \times c_{filler}}{\rho_{filler}}$$

where m, c_{PCL}, c_{filler}, ρ_{PCL}, and ρ_{filler} is the actually measured mass of the specimens, the weight percentage of the pure PCL matrix, the weight percentage of the reinforcing filler (AlN-30 or BN-30), the density of the pure PCL matrix, and the density of the reinforcing filler (AlN-30 or BN-30), respectively.

3. Results and discussion

The weakest points inside the fabricated parts should be paid attention to when taking practical applications into account. It is meaningful to characterize the mechanical properties of the fabricated FGC specimens as a whole part, although the various properties of the inner-layers are considerably different from each other, such as the thermal conductivity [7]. The type of *m*-FDM 3D printed samples were separately listed in Table 1. For convenience without specification, the FGC sample ID (A, B, C, D, E, F, and G) was employed to mark the samples named in Table 1 in the following study.

The interlayer adhesion or bonding strength between two adjacent deposition roads relies on the molecular thermal diffusion at the interfaces [13], which means that the more molecular entanglement and diffusion would give rise to better bonding strength and thus higher mechanical properties. The interfaces between two nearby layers can be considered as the weakest points for the *m*-FDM 3D printed specimens, comparing to the material itself. According to the crack propagation mechanism, the cracks always propagate along with the weakest points when loading. In consideration of the loading direction acting on the inhomogeneous (i.e. the *m*-FDM 3D printed FGC) parts, an interesting phenomenon happens, as illustrated in Fig. 1. Fig. 1a indicates the load-displacement relationship of the FGC parts with mechanical gradients. A platform can be observed on the curve of Sample D and F, indicating that the force transfers downward to the pure PCL side when loading, which leads to the tensile failure of downside after the shear failure, and thus consumes more energy. It is worth noting that the tensile failure of Sample D and F only occurs after the shear failure, while there is no tensile failure observed after shear failure for the Sample E and G. Also, the load used to calculate the ILSS was the force when shear failure occurred (particularly, before tensile failure for the Sample D and F). The photos of D and E after the ILSS test (see the insets in Fig. 1a) show that the downside of the Sample D fractures while there are cracks in the interlayers of the Sample E, which verifies the explanation above. As a result, when the pure PCL side contacts the pedestal (i.e. Sample D and F, the loading direction is from PCL-based composites to PCL), the ILSS is almost two times of the one when the pure PCL side contacts the pressure head (i.e. Sample E and G, the loading direction is from PCL to PCL-based composites), under both cases of AlN-30 and BN-30. However, as observed in Fig. 1b, when adding 70 wt% of AlN-30 or 50 wt% of BN-30 particles, the dispersion is difficult and agglomeration is significant (see Fig. S1 in the Supporting Information), leading to the stress concentration in the samples (Sample B, C, D, E, F, and G) [23]. On the other hand, the PCL matrix (the highest ILSS) is too little to transfer stress effectively, resulting in the lower ILSS.

Table 1
The type of *m*-FDM 3D printed samples.

Sample ID	Type
A	PCL
B	PCL/AlN-30(70 wt%)
C	PCL/BN-30(50 wt%)
D	PCL/AlN-30(70 wt%) → PCL[a]
E	PCL → PCL/AlN-30(70 wt%)
F	PCL/BN-30(50 wt%) → PCL
G	PCL → PCL/BN-30(50 wt%)

[a] The "→" represents the loading direction acting on the mechanical gradient samples.

Fig. 2 reveals the change of the storage modulus for different samples mentioned in Table 1. Different from the ILSS results, by introducing the AlN-30 powders, the storage modulus is nearly 715 MPa (Sample E) and 650 MPa (Sample D) when the pure PCL side is contacting (Sample E) and far away from the pressure head (Sample D), respectively. The same trend can be found in Sample F and G. It merely shows that the storage modulus of the several top layers as the thickness of the tested specimens for DMA approaches 2 mm. However, the polymer chains possess large free volume at high temperature, giving rise to a decrease in the storage modulus [24].

To further investigate the relationship between structures and mechanical properties of the *m*-FDM 3D printed FGC parts with mechanical gradients, the samples with different linearly continuous gradients of filler content were prepared, where the n_L represents the deposited layers which is fixed at 10 in this study. The loading direction in the tensile test is perpendicular to the deposited direction, so there is no effect of the loading direction on the tensile properties. As illustrated in Fig. 3, the influence of the gradient of filler content on the tensile strength is significant, presenting a peak in the tensile curve when the gradient of filler content is 3 wt%/n_L and 2 wt%/n_L for PCL/AlN-30 and PCL/BN-30 composites, respectively. In other words, the filler content for the best tensile strength is around 30 wt% and 20% wt% for PCL/AlN-30 and PCL/BN-30 composites, where the tensile strength is improved by about 32.8% (PCL/AlN-30) and 39.1% (PCL/BN-30) comparing to the pure PCL (0 wt%/n_L in Fig. 3). It might be due to the rigidity of the reinforcing fillers, working similarly to the reinforcing materials. The rigid fillers (AlN-30 and BN-30) can restrict the movement of the PCL molecular chains and make the samples endure larger loading without deformation, leading to higher modulus as well as strength. When adding slight reinforcing filler powders, the cracks would propagate along with the surfaces of the reinforcing particles (AlN-30 or BN-30) inside the deposited lines, which lengthens the crack paths and thus consumes more energy [25–27]. When the gradient of filler content is more than 3 wt%/n_L in the *m*-FDM 3D-printed PCL/AlN-30 (or 2 wt%/n_L in the *m*-FDM 3D-printed PCL/BN-30) FGC parts, the dispersibility reduces and the aggregation increases (see Fig. S1 in the Supporting Information), which makes the stress concentration happen in the *m*-FDM 3D printed FGC parts. The phenomenon becomes remarkable as the content of the reinforcing filler (AlN-30 or BN-30) further rises.

The effect of the gradient of filler content on the porosity was further presented in Fig. 4. The results in Fig. 4 show that the porosity of the samples with 0 and 7 wt%/n_L gradient of filler content is 9.0% and 14.6%, respectively, which can be also intuitively realized from the SEM images (the inset I and III in Fig. 4). In addition, the overall porosity of printed samples increases linearly with increasing the gradient of filler content. And the increasing rate of the curve of BN-30 is greater than that of AlN-30. There are two kinds of voids existing in the *m*-FDM 3D printed samples, including the gaps between the reinforcing particles and the PCL matrix and the physical voids at the interfaces between two neighbor deposited layers [22]. The first type of voids (the gaps between the reinforcing particles and the PCL matrix) is mainly created during the manufacturing of the feedstock filaments in the extruding process executed on the single-screw extruder. While the second type of voids (the physical voids at the layer/layer interfaces) mainly results from the *m*-FDM 3D printing process, which accounts for a higher proportion. The reinforcing fillers (AlN-30 or BN-30 particles) decrease the die-swell effect of the PCL molecules and restrain the movement of the molecules, so the deposited PCL/filler composite layers tend to sustain circular shape, resulting in the bigger voids and thus the poorer adhesion strength between two adjacent deposited lines or layers [28]. Meanwhile, the inter-particle voids store up. Moreover, due to the irregular planar shape of BN-30, the voids become much bigger during the FDM process, giving rise to a greater increase in the porosity. As a result, the tensile strength decreases sharply as the reinforcing particles (AlN-30 or

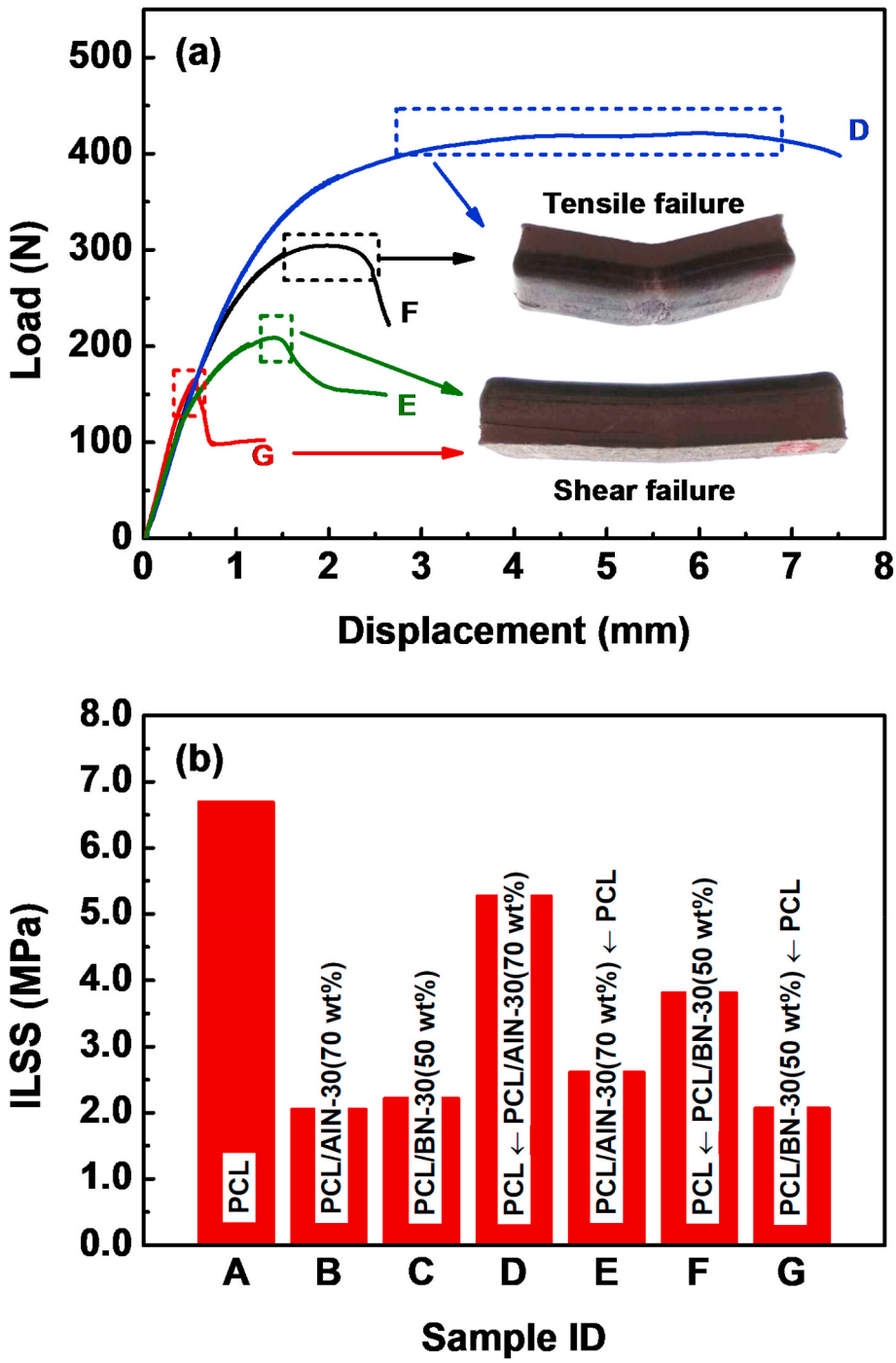

Fig. 1. (a) The load-displacement curves of the inhomogeneous parts (Sample D, E, F, and G) during the ILSS test. (b)The ILSS of the *m*-FDM 3D printed FGC parts with different mechanical gradients (Sample A, B, C, D, E, F, and G). The samples A-G correspond to the samples A-G in Table 1.

BN-30) increase (see Fig. 3).

Based on the above examinations on the mechanical properties and our previous research on the thermal conductive properties of the *m*-FDM 3D printed PCL-based FGC parts [7], both the structure and property parameters show continuous variations, which can effectively enhance the mechanical strength of the materials in the interface area. Also, each side of the same materials has distinctive properties or diverse functions, which can achieve the matching performance without failure under harsh service conditions. Due to the difference in the expansion coefficient between the two incompatible or different materials, the huge thermal stress will come into being when used at high temperatures, resulting in spalling on the material surfaces and the failure of the materials. The FGMs with functional or performance gradients can connect two incompatible or different materials to improve the interfacial bonding strength and reduce the residual stress that cracks the two different materials. Fig. 5 exhibits one potential application of FGMs as the intermediate layers between Al foil and PVC film molded by heat laminating. The circular ring with various wall thicknesses was fabricated by *m*-FDM 3D printing, with increasing the AlN-30 powders from the outside to the inside. Because of the huge difference in the thermal expansion coefficient between Al and PVC, the two materials will warp and then spall when heating. The functionally gradient intermediate layers can effectively relieve the problem and simultaneously achieve the optimal effect of the heat and stress transfer.

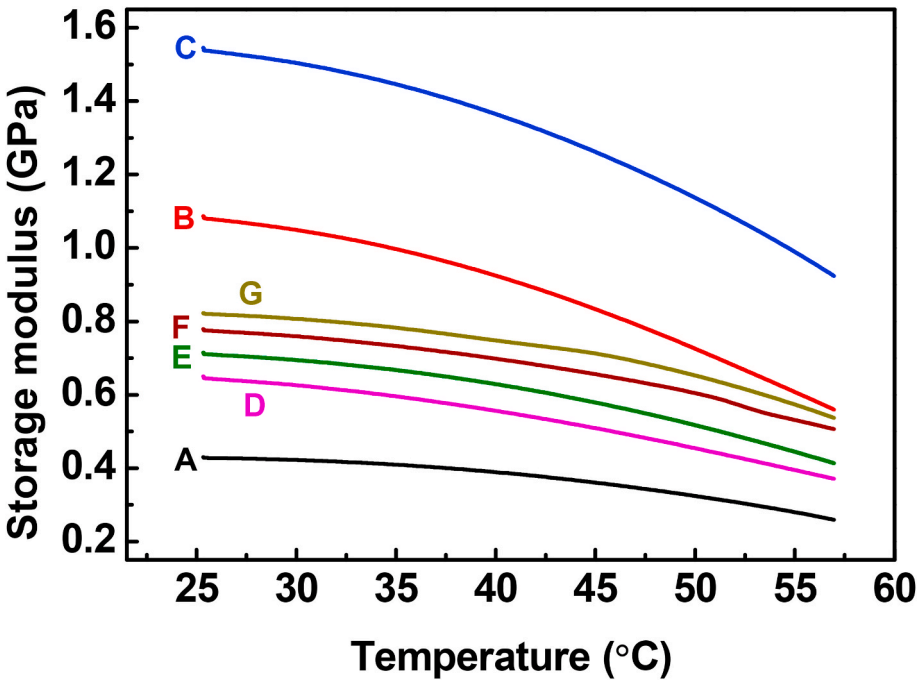

Fig. 2. The variation of storage modulus of different samples with temperature through the DMA test. The samples A-G correspond to the samples A-G in Table 1.

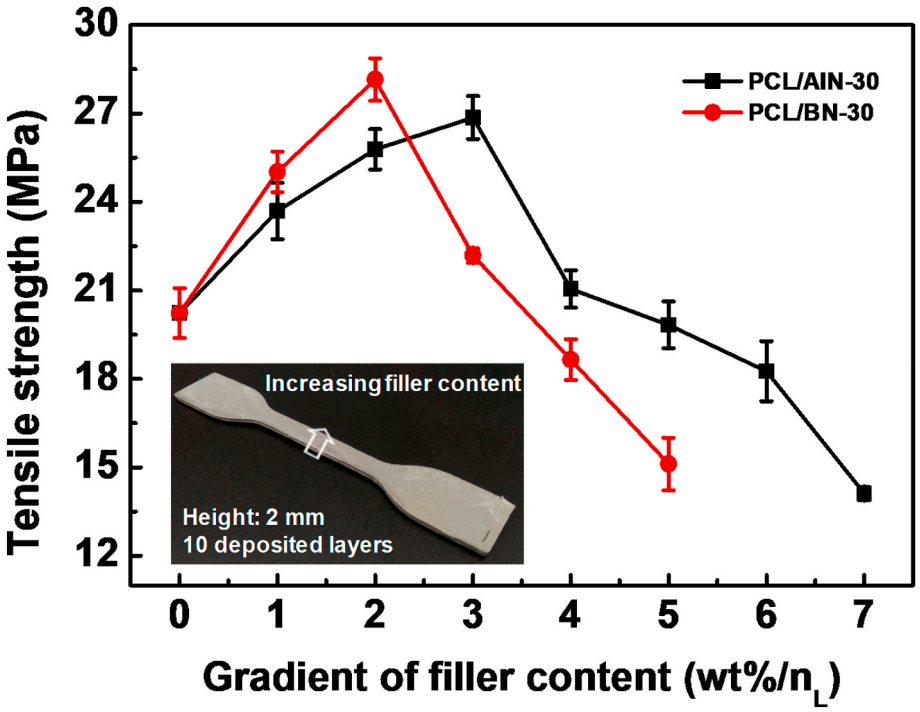

Fig. 3. The effect of the gradient of filler content on the tensile strength of the functionally gradient PCL/AIN-30 composites and PCL/BN-30 composites, where the 0 wt%/n_L gradient of filler content represents the pure PCL.

4. Conclusions

A multi-material FDM 3D printing technology was proposed to prepare the functionally gradient composite (FGC) parts with diversely tunable mechanical gradients. The mechanical properties of the fabricated FGC samples were studied as an integral, which establishes the relationship between structures and properties of the thermoplastic FGC parts. It was found that the loading direction plays a key role in the ILSS and storage modulus. When the loading direction is from PCL-based (PCL/AlN-30 or PCL/BN-30) composites to PCL, the ILSS shows higher while the storage modulus lower than that from PCL to PCL-based composites. The relationship between structures and mechanical properties of FGC parts with different linearly continuous gradients of filler content were further investigated, indicating that the influence of the gradient of filler content on the tensile strength is significant, where the tensile strength firstly increases upward to the highest (at 3 wt%/n_L for PCL/AlN-30 and 2 wt%/n_L for PCL/BN-30) and then decreases. As compared to the pure PCL (0 wt%/n_L), the tensile strength is improved

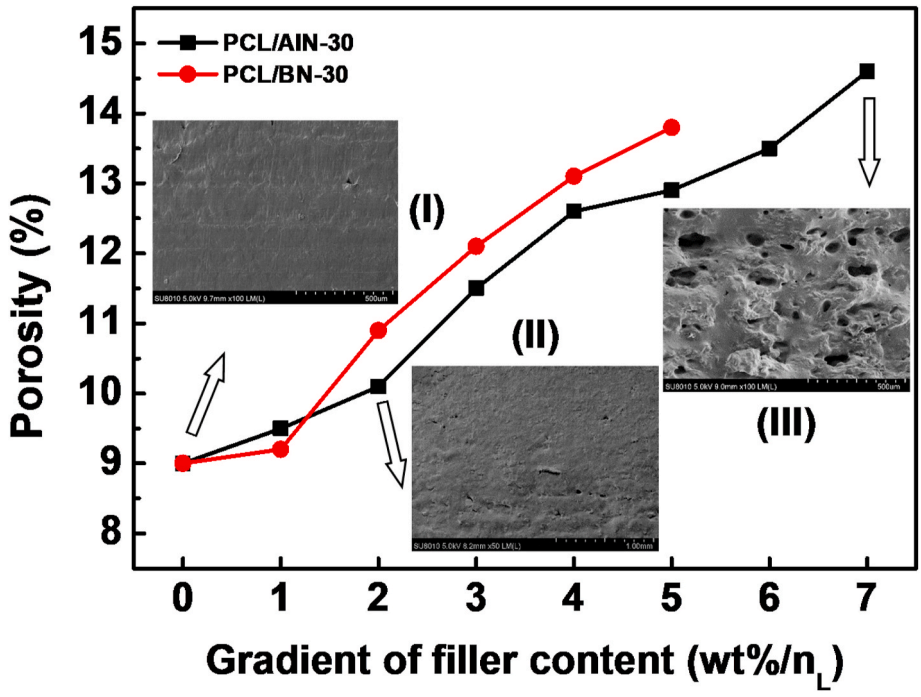

Fig. 4. The effect of the gradient of filler content on the porosity of the functionally gradient PCL/AlN-30 and PCL/BN-30 composites, where the 0 wt%/n_L gradient of filler content represents the pure PCL. The inset I, II, and III represent the SEM photography for the pure PCL, PCL/AlN-30 composites at 2 wt%/n_L, and PCL/AlN-30 composites at 7 wt%/n_L, respectively.

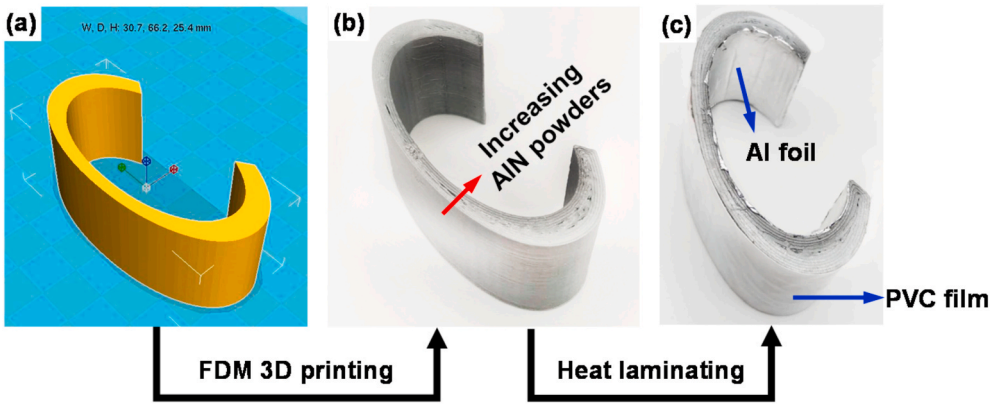

Fig. 5. The potential practical application of the FGC part with PCL/AlN-30 by FDM 3D printing: (a) designed model with different gradients, (b) *m*-FDM 3D printed intermediate layer of functionally gradient PCL/AlN-30 composites, and (c) functionally gradient PCL/AlN-30 composites as the intermediate layer between Al foil and PVC film.

by about 32.8% (PCL/AlN-30) and 39.1% (PCL/BN-30). According to the effect of the gradient of filler content on the porosity, it can be convinced that the tensile strength of the *m*-FDM 3D printed FGC parts with diverse mechanical gradients is influenced by the gaps between the reinforcing fillers (AlN-30 or BN-30) and the PCL matrix as well as the physical voids at layer/layer interfaces simultaneously. Finally, the potential practical application as the intermediated layers between two incompatible materials (e.g. Al foil and PVC film) with a huge difference in the thermal expansion coefficient was further designed, which helps to lay a theoretical foundation of the other practical applications in diverse fields.

CRediT authorship contribution statement

Xu Zhang: Conceptualization, Investigation, Data curation, Writing - original draft, Writing - review & editing. **Jianlei Wang:** Methodology, Resources, Software, Data curation, Visualization, Writing - review & editing. **Tianxi Liu:** Supervision, Project administration, Funding acquisition.

Declaration of competing interest

The authors declare that they have no known competing financial interests or personal relationships that could have appeared to influence the work reported in this paper.

Acknowledgements

This work was financially supported by the Fundamental Research Funds for the Central Universities (Grant No.: 2232020D-11 and 2232019A3-03) and the National Natural Science Foundation of China (Grant No.: 21674019 and 21875033).

Appendix A. Supplementary data

Supplementary data to this article can be found online at https://doi.org/10.1016/j.coco.2020.100600.

References

[1] C. Ortiz, M.C. Boyce, Bioinspired structural materials, Science 319 (2008) 1053–1054.

[2] L. Rossetti, L.A. Kuntz, E. Kunold, J. Schock, K.W. Müller, H. Grabmayr, J. Stolberg-Stolberg, F. Pfeiffer, S.A. Sieber, R. Burgkart, A.R. Bausch, The microstructure and micromechanics of the tendon-bone insertion, Nat. Mater. 16 (2017) 664–670.

[3] J. Aizenberg, J.C. Weaver, M.S. Thanawala, V.C. Sundar, D.E. Morse, P. Fratzl, Skeleton of *Euplectella* sp.: structural hierarchy from the nanoscale to the macroscale, Science 309 (2005) 275–278.

[4] A. Miserez, T. Schneberk, C. Sun, F.W. Zok, J.H. Waite, The transition from stiff to compliant materials in squid beaks, Science 319 (2008) 1816–1819.

[5] D.K. Kim, W. Woo, E.Y. Kim, S.H. Choi, Microstructure and mechanical characteristics of multi-layered materials composed of 316L stainless steel and ferritic steel produced by direct energy deposition, J. Alloys Compd. 774 (2019) 896–907.

[6] K.A. Bhaskararao, G.R. Janardhana, Influence of Al2O3 and ZrO2 alloying on microstructure, hardness and flexural strength of Ni based functionally graded composites by vacuum sintering, Compos Commun 22 (2020), 100458.

[7] J. Wang, S. Mubarak, D. Dhamodharan, N. Divakaran, L. Wu, X. Zhang, Fabrication of thermoplastic functionally gradient composite parts with anisotropic thermal conductive properties based on multicomponent fused deposition modeling 3D printing, Compos Commun 19 (2020) 142–146.

[8] K. Kokini, J. DeJonge, S. Rangaraj, B. Beardsley, Thermal shock of functionally graded thermal barrier coatings with similar thermal resistance, Surf. Coating. Technol. 154 (2002) 223–231.

[9] F. Watari, A. Yokoyama, M. Omori, T. Hirai, H. Kondo, M. Uo, T. Kawasaki, Biocompatibility of materials and development to functionally graded implant for bio-medical application, Compos. Sci. Technol. 64 (2004) 893–908.

[10] M. Herrmann, W. Sobek, Functionally graded concrete: numerical design methods and experimental tests of mass-optimized structural components, Struct. Concr. 18 (2017) 54–66.

[11] D. Fabris, J.C.M. Souza, F.S. Silva, M. Fredel, J. Mesquita-Guimarães, Y. Zhang, B. Henriques, The bending stress distribution in bilayered and graded zirconia-based dental ceramics, Ceram. Int. 42 (2016) 11025–11031.

[12] X. Zhang, W. Fan, T. Liu, Fused deposition modeling 3D printing of polyamide-based composites and its applications, Compos Commun 21 (2020), 100413.

[13] X. Zhang, J. Wang, Controllable interfacial adhesion behaviors of polymer-on-polymer surfaces during fused deposition modeling 3D printing process, Chem. Phys. Lett. 739 (2020), 136959.

[14] Y. Guo, J. Xu, C. Yan, Y. Chen, X. Zhang, X. Jia, Y. Liu, X. Wang, F. Zhou, Direct ink writing of high performance architecture polyimides with low dimensional shrinkage, Adv. Eng. Mater. 21 (2019), 1801314.

[15] X. Kuang, J. Wu, K. Chen, Z. Zhao, Z. Ding, F. Hu, D. Fang, H.J. Qi, Grayscale digital light processing 3D printing for highly functionally graded materials, Sci Adv 5 (2019), eaav5790.

[16] M.J. Mirzaali, A. Heranz de la Nava, D. Gunashekar, M. Nouri-Goushki, R.P. E. Veeger, Q. Grossman, L. Angeloni, M.K. Ghatkesar, L.E. Fratila-Apachitei, D. Fuffoni, E.L. Doubrovski, Zadpoor, Mechanics of bioinspired functionally graded soft-hard composites made by multi-material 3D printing, Compos. Struct. 237 (2020), 111867.

[17] X. Peng, M. Zhang, Z. Guo, L. Sang, W. Hou, Investigation of processing parameters on tensile performance for FDM-printed carbon fiber reinforced polyamide 6 composites, Compos Commun 22 (2020), 100478.

[18] V. Tambrallimath, R. Keshavamurthy, D. Saravanabavan, P.G. Koppad, G.S. P. Kumar, Thermal behavior of PC-ABS based graphene filled polymer nanocomposite synthesized by FDM process, Compos Commun 15 (2019) 129–134.

[19] L. Li, Y. Chen, T. Yu, N. Wang, C. Wang, H. Wang, Preparation of polylactic acid/TEMPO-oxidized bacterial cellulose nanocomposites for 3D printing via Pickering emulsion approach, Compos Commun 16 (2019) 162–167.

[20] Y. Ming, Z. Xin, J. Zhang, Y. Duan, B. Wang, Fabrication of continuous glass fiber-reinforced dual-cure epoxy composites via UV-assisted fused deposition modeling, Compos Commun 21 (2020), 100401.

[21] P.A.G.S. Giachini, S.S. Gupta, W. Wang, D. Wood, M. Yunusa, E. Baharlou, M. Sitti, A. Menges, Additive manufacturing of cellulose-based materials with continuous, multidirectional stiffness gradients, Sci Adv 6 (2020), eaay0929.

[22] J. Wang, T. Senthil, L. Wu, X. Zhang, Enhancement of lightweight composite parts with robust cellular structures by combining fused deposition modeling and electromagnetic induction heating, Adv. Eng. Mater. 20 (8) (2018), 1800215.

[23] A.L. Yesgat, R. Kitey, Effect of filler geometry on fracture mechanisms in glass particle filled epoxy composites, Eng. Fract. Mech. 160 (2016) 22–41.

[24] J. Wang, H. Xie, Z. Weng, T. Senthil, L. Wu, A novel approach to improve mechanical properties of parts fabricated by fused deposition modeling, Mater. Des. 105 (2016) 152–159.

[25] W.G. Jiang, S.R. Hallett, B.G. Green, M.R. Wisnom, A concise interface constitutive law for analysis of delamination and splitting in composite materials and its application to scaled notched tensile specimens, Int. J. Numer. Methods Eng. 69 (9) (2007) 1982–1995.

[26] B.D. Le, F. Dau, J.L. Charles, I. Iordanoff, Modeling damages and cracks growth in composite with a 3D discrete element method, Compos. B Eng. 91 (2016) 615–630.

[27] J. Sun, Z. Jing, J. Wu, W. Wang, D. Zhang, J. Zhao, Strain rate effects on dynamic tensile properties of open-hole composite laminates, Compos Commun 19 (2020) 229–232.

[28] M. Nikzad, S.H. Masood, I. Sbarski, Thermo-mechanical properties of a highly filled polymeric composites for fused deposition modeling, Mater. Des. 32 (6) (2011) 3448–3456.